VLBI IMAGING OF THE DOUBLE PEAKED EMISSION LINE SEYFERT KISSR 1494

P. Kharb[1], M. Das[1], Z. Paragi[2], S. Subramanian[1], and L. P. Chitta[1]
[1] Indian Institute of Astrophysics, II Block, Koramangala, Bangalore 560034, India; kharb@iiap.res.in
[2] Joint Institute for VLBI in Europe, Postbus 2, 7990 AA Dwingeloo, The Netherlands

ABSTRACT

We present here the results from dual-frequency phase-referenced Very Long Baseline Interferometry observations of the Seyfert galaxy KISSR 1494, which exhibits double peaked emission lines in its Sloan Digital Sky Survey spectrum. We detect a single radio component at 1.6 GHz, but not at 5 GHz, implying a spectral index steeper than -1.5 ± 0.5 ($S_\nu \propto \nu^\alpha$). The high brightness temperature of the radio component ($\sim 1.4 \times 10^7$ K) and the steep radio spectrum support a non-thermal synchrotron origin. A crude estimate of the black hole mass derived from the $M_{\rm BH}$–$\sigma_\star$ relation is $\sim 1.4 \pm 1.0 \times 10^8\ M_\odot$; it is accreting at an Eddington rate of ~ 0.02. The radio data are consistent with either the radio emission coming from the parsec-scale base of a synchrotron wind originating in the magnetized corona above the accretion disk, or from the inner ionized edge of the accretion disk or torus. In the former case, the narrow line region (NLR) clouds may form a part of the broad outflow, while in the latter, the NLR clouds may form a part of an extended disk beyond the torus. The radio and NLR emission may also be decoupled so that the radio emission originates in an outflow while the NLR is in a disk and vice versa. While with the present data it is not possible to clearly distinguish between these scenarios, there appears to be greater circumstantial evidence supporting the coronal wind picture in KISSR 1494. From the kiloparsec-scale radio emission, the time-averaged kinetic power of this outflow is estimated to be $Q \approx 1.5 \times 10^{42}$ erg s^{-1}, which is typical of radio outflows in low-luminosity active galactic nuclei. This supports the idea that radio "jets" and outflowing coronal winds are indistinguishable in Seyfert galaxies.

Key words: galaxies: individual (KISSR 1494) – galaxies: nuclei – galaxies: Seyfert – radio continuum: galaxies

1. INTRODUCTION

It is now widely believed that all luminous galaxies host supermassive black holes (SMBH; $M_{\rm BH} \sim 10^6$–$10^9\ M_\odot$) in their centers (e.g., Kormendy & Ho 2013). Since mergers are an essential part of the evolutionary process of a galaxy (e.g., Barnes & Hernquist 1992), the presence of multiple SMBH in galactic nuclei are expected (e.g., Volonteri et al. 2003). However, so far, there are only 18 confirmed dual/binary accretion-powered active galactic nuclei (AGNs) known in the literature (Deane et al. 2014). Only three of these systems have black hole (BH) separations <1 kpc. These are 0402+379 (BH separation ∼7 pc; Rodriguez et al. 2006), NGC 6240 (BH separation ∼70 pc; Komossa et al. 2003), and NGC 3393 (BH separation ∼150 pc; Fabbiano et al. 2011). The dual AGN candidate (with a BH separation of ∼77 pc) identified by Gitti et al. (2013) in the galaxy cluster RBS 797 needs to be confirmed by multi-frequency radio imaging which should ideally detect two flat spectrum radio cores (e.g., see Burke-Spolaor 2011). However, as pointed out by Wrobel et al. (2014), single young AGNs may show double radio structures with relatively compact flat spectrum "hot spots" that may be mistaken for dual AGN cores in sensitivity-limited observations.

Almost all of the dual/binary AGN candidates (see Deane et al. 2014) reside in merger remnants or elliptical galaxies, with the rare exception of NGC 3393, which resides in a spiral galaxy (Fabbiano et al. 2011). The merger process, which creates large elliptical galaxies (e.g., Steinmetz & Navarro 2002), results in gas infall, massive star formation, and the formation of supermassive BH binaries. Spiral galaxies, on the other hand, undergo minor mergers (e.g., satellite accretion), which result in larger bulges and intact disks (Aguerri et al. 2001): binary SMBH must therefore be rarer in spiral galaxies.

There are attempts in the literature to identify a greater number of dual/binary AGNs. One of the adopted techniques is via the identification of AGNs with double-peaked emission lines (DPAGNs), with the assumption that the split in the emission lines is a consequence of two BHs carrying along with them their respective narrow/broad emission line regions (NLR/BLR) having different characteristic velocities. While some DPAGNs have indeed turned out to be dual AGNs (e.g., Fu et al. 2011), it is becoming apparent that this technique is not necessarily more efficient in detecting binary BHs than other techniques like identifying sources with S- or X-shaped jets. For instance, Fu et al. (2012) discovered only two binary AGNs in a sample of 42 DPAGNs. As is becoming clear in more and more sources, double-peaked emission lines could result from radio outflows and jet–medium interaction (e.g., Rosario et al. 2010; Fischer et al. 2011; Gabányi et al. 2014), or rotating gaseous disks (e.g., Shen et al. 2011; Smith et al. 2012). Nevertheless, the search for binary BHs in DPAGNs goes on.

Both the *Chandra X-Ray Observatory* and the *Hubble Space Telescope* have been instrumental in the identification and confirmation of dual AGNs with kiloparsec-scale BH separations (e.g., Komossa et al. 2003; Fabbiano et al. 2011). However, Deane et al. (2014) have noted that >60% of the sub-10 kpc dual/triple AGN candidates have associated radio emission: BH activity and radio jet formation are enhanced in systems with two or more BHs, which are a consequence of mergers. The technique of Very Long Baseline Interferometry (VLBI) is essential to identify and confirm radio-emitting binary AGNs with parsec-scale BH separations: multiple frequencies must be used to check if the core spectra are flat/inverted.

Seyfert galaxies have traditionally been identified as "radio-quiet" AGNs (however, see Ho & Peng 2001; Kharb et al. 2014a). Therefore, the detection of a binary radio-emitting
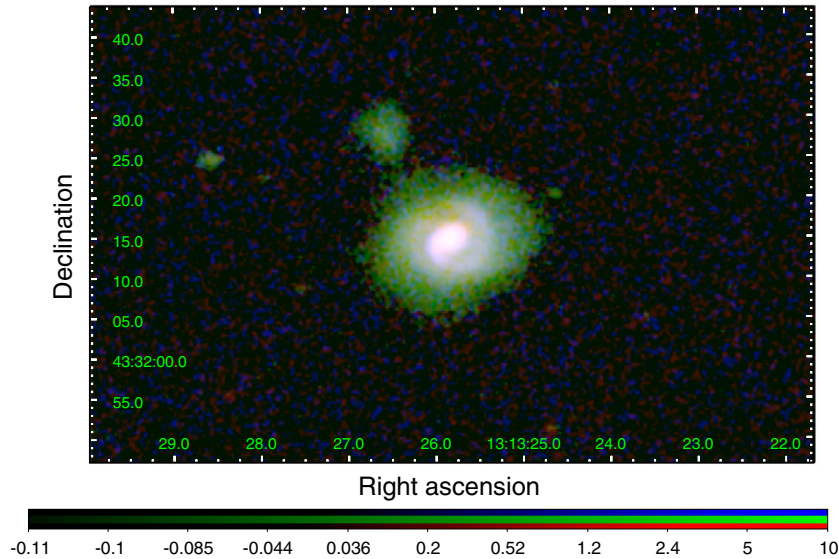
Figure 1. RGB image of KISSR 1494 made using z (central $\lambda = 9134$ Å), r (= 6231 Å), and u (= 3543 Å) filters of the SDSS.

AGN in a Seyfert nucleus is doubly challenging. In the current paper, we present results from VLBI observations of a Seyfert galaxy with double peaked emission lines in its Sloan Digital Sky Survey (SDSS) spectrum. However, before discussing this source, it is worth discussing the complex nature of radio emission in Seyfert galaxies.

Unlike the outflows in powerful radio galaxies, Seyfert outflows are a poorly understood phenomenon. Only sensitive radio observations at low radio frequencies reveal the presence of radio structures with typical extents $\lesssim$10 kpc in Seyfert galaxies. Gallimore et al. (2006) and Singh et al. (2015) have found that $\gtrsim$40% of Seyferts belonging to large (complete or eclectic) samples exhibit kiloparsec-scale radio structures when observed with sensitive radio arrays (e.g., Very Large Array, VLA, in the D-array configuration). It is unclear *how* or *where* these radio outflows are generated. The contribution of the AGN versus star-formation to the radio emission is also debatable (e.g., Baum et al. 1993; Hota & Saikia 2006). Malzac et al. (2001) and Markoff et al. (2005) have argued the case for Seyfert outflows being outflowing accretion-disk coronae. High resolution VLBI observations, on the other hand, have detected the presence of parsec-scale jets in a majority of radio-bright Seyferts (e.g., Nagar et al. 2005; Kharb et al. 2010, 2014a; Mezcua & Prieto 2014). The VLBI cores however do not always exhibit flat/inverted spectra and could have steep spectra instead (e.g., Roy et al. 2000; Orienti & Prieto 2010; Kharb et al. 2010; Bontempi et al. 2012; Panessa & Giroletti 2013), unlike the unresolved bases of relativistic jets in powerful radio galaxies.

We present here the results from multi-frequency Very Long Baseline Array (VLBA) observations of the Seyfert 2 galaxy KISSR 1494 belonging to the KPNO Internal Spectroscopic Survey (KISS) of spiral/disk emission line galaxies (Wegner et al. 2003). KISS is a nearly complete sample of emission-line galaxies over a well-defined volume in space. The survey was carried out using the 2.4 m MDM telescope on Kitt Peak and contains 351 galaxies. We searched through the KISS sample for signatures of double peaked emission line AGNs. We examined the SDSS[3] spectra of those galaxies which had been classified as either Seyfert 1, Seyfert 2, or LINER[4] (a total of 72 galaxies),

and identified six (i.e., 8%) as having double peaks in their emission line spectra. Only three of these, e.g., KISSR 434, KISSR 1219, and KISSR 1494, had been detected in the VLA FIRST[5] and NVSS[6] surveys at 1.4 GHz (resolution $\sim$5″.4 and $\sim$45″, respectively). KISSR 1494 was the brightest of these three with an integrated flux density of $\sim$23 mJy and $\sim$25 mJy in the FIRST and NVSS images, respectively. The focus on KISSR 1494 in this paper therefore merely stems from the fact that it is bright enough to be observed with VLBI.

KISSR 1494 has a high *IRAS* 100 μm flux density ($\sim$4.8 Jy) and soft X-ray (0.1–2.4 keV) luminosity in the *ROSAT* sky survey ($L_{\rm X} = 1.05 \times 10^{42}$ erg s^{-1}; Stevenson et al. 2002). The X-ray luminosity was derived for an absorbed power-law model with $\Gamma = 2.5$ and $N_{\rm H}$ = Galactic + (2.0 $\times 10^{20}$) cm^{-2}. The SDSS image of KISSR 1494 reveals a disky structure, a prominent bulge, and a one-armed spiral feature (Figure 1). A one-armed spiral indicates an $m = 1$ instability which could arise due to counter-rotating gas/stars (e.g., Zang & Hohl 1978). One explanation for such counter-rotating material could be the ingestion of small galaxy, small enough to not have destroyed the spiral structure of the larger galaxy.

The SDSS spectrum of KISSR 1494 shows several emission lines that are characteristic of AGN activity, the most prominent being Hα, Hβ, and [O III].[7] The Hα, Hβ, and Hγ lines have distinct double peaks (Figures 2 and 3). As the two components of the narrow Hα, Hβ lines have nearly equal strength, this source can be classified as an equal-peaked AGN (Smith et al. 2012). Traces of double peaks are also observed in the [S II], [O I], and [O II] lines. The [N II] and [O III] lines appear broad and asymmetric, possibly due to blended double peaks.

At the KISSR 1494 redshift of $z = 0.057446$ (luminosity distance, $D_L = 250$ Mpc), 1 milliarcsec (mas) corresponds to a linear extent of 1.08 pc for $H_0 = 73$ km s^{-1} Mpc^{-1}, $\Omega_{\rm mat} = 0.27$, $\Omega_{\rm vac} = 0.73$. The spectral index, α, is defined throughout such that the flux density at frequency ν is $S_\nu \propto \nu^\alpha$.

---

[3] Sloan Digital Sky Survey; https://www.sdss3.org/dr10.
[4] Low-Ionization Nuclear Emission-line Region galaxies.

[5] Faint Images of the Radio Sky at Twenty-Centimeters; http://sundog.stsci.edu.
[6] The NRAO VLA Sky Survey; http://www.cv.nrao.edu/nvss.
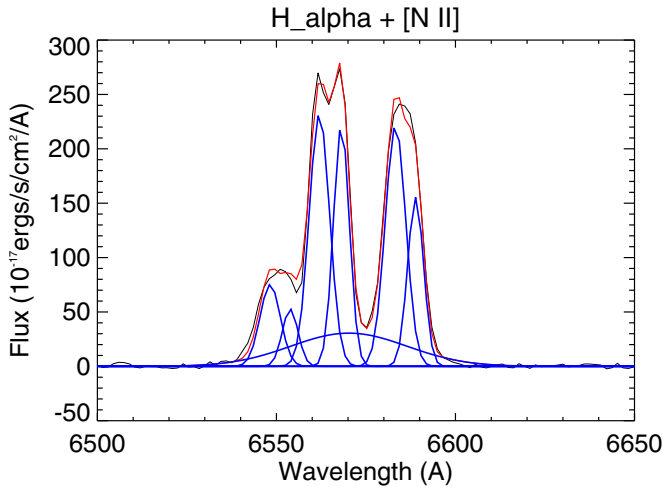[7] The SDSS spectra are acquired through a fiber of diameter 3″, or 3.24 kpc at the distance of KISSR 1494.

Figure 2. SDSS spectrum of KISSR 1494 showing the dereddened double-peaked Hα+[N II] lines in black, Gaussian line fits in blue, and the total spectrum in red.

2. OBSERVATIONS AND DATA REDUCTION

2.1. Phase-referenced VLBI

The observations were carried out with nine antennas of the VLBA at 1.55 and 4.98 GHz, on 2013 August 10 (Project ID: BK182); the Fort Davis antenna was not involved in the experiment. Fringes were not detected with the Pie Town antenna.

Therefore, effectively only eight antennas of the VLBA were used for the observations. The data were acquired with an aggregate bit rate of 1024 Mbits s^{-1} (two polarization, two baseband channels, bandwidth 128 MHz, and a two-bit sampling rate), in a phase-referencing mode. 1325+436, which is 2°53 away from the source and has an x, y positional uncertainty of 0.18, 0.28 mas, was used as the phase reference calibrator. 3C 345 and 1315+415 were used as the fringe-finder and phase-check calibrator, respectively. A nodding cycle of 5 minutes (2 minutes on the phase calibrator and 3 minutes on the target) was used for the observations, interspersed by two 5 minute scans on 3C 345 and two 3 minute scans on the phase-check calibrator (only a single scan of the latter at 5 GHz). The experiment lasted a total of three hours, with ≈1.5 hr at each frequency.

The data reduction was carried out using Astronomical Image Processing System (AIPS; version 31DEC12) following standard VLBA-specific tasks and procedures outlined in the AIPS cookbook.[8] Los Alamos, which was a stable antenna in the middle of the configuration, was used as the reference antenna for the calibration. The amplitude calibration was carried out using the procedure VLBACALA, while the delay, rate, and phase calibration were carried out using the procedures VLBAPANG, VLBAMPCL and VLBAFRGP. The phase calibrator 1325+436 was iteratively imaged and self-calibrated on both phase and phase+amplitude using AIPS tasks IMAGR and CALIB.
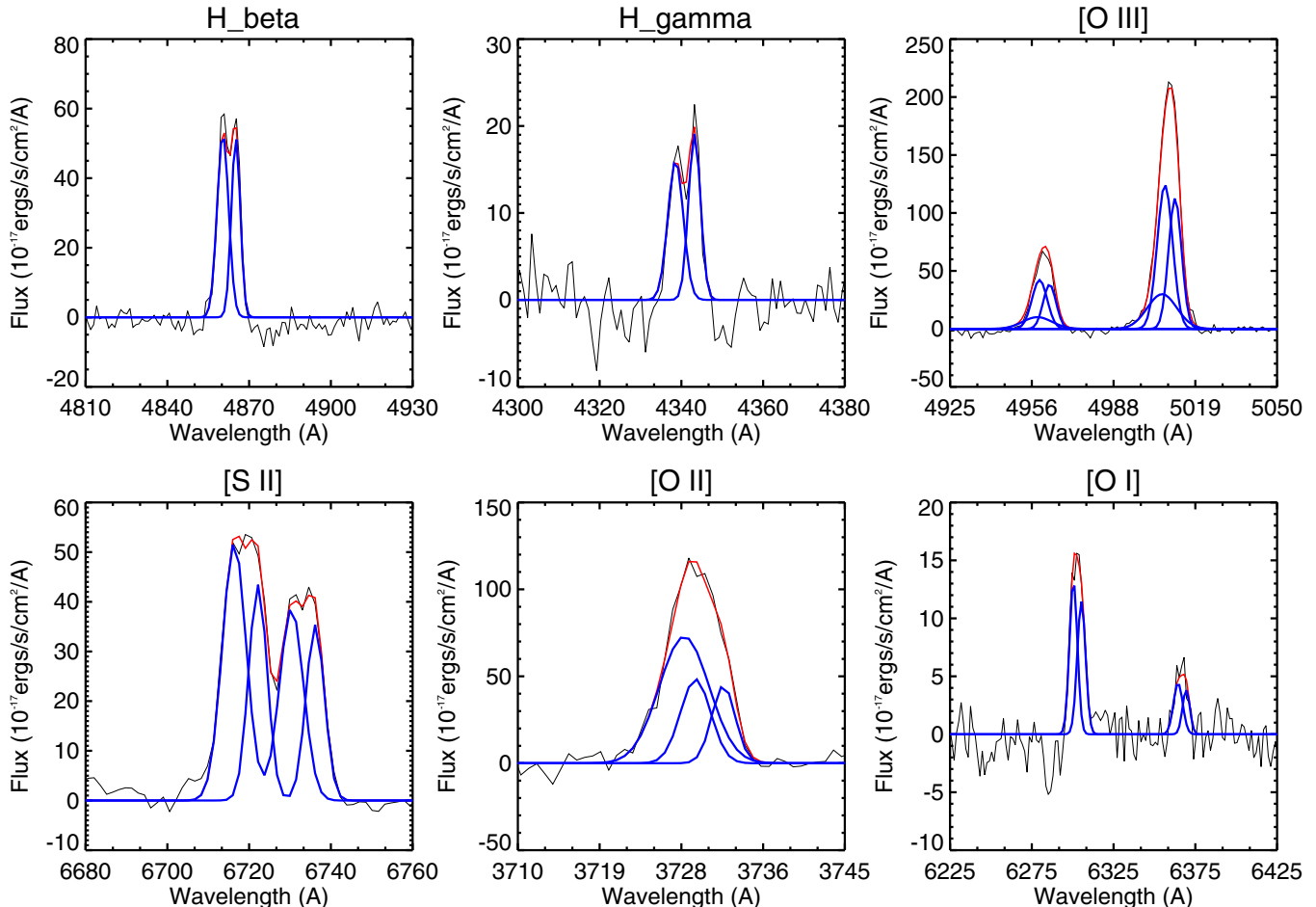
---

[8] http://www.aips.nrao.edu/cook.html

Figure 3. SDSS spectrum of KISSR 1494 showing the dereddened double-peaked Hβ, Hγ, [S II], [O I] lines, and the asymmetric [O II], [O III] lines in black. The Gaussian line fits are shown in blue and the total spectrum in red.

The images were then used as models to determine the amplitude and phase gains for the antennas. These gains were applied to the target and the final images were made using `IMAGR`. A round of data-flagging was carried out using the task `IBLED` on the source `SPLIT` file, prior to making the images. The radio component detected at 1.6 GHz was offset from the center of the image by $0\rlap{.}''076$, $0\rlap{.}''120$ in right ascension and declination. We ran the task `UVFIX` on the source `SPLIT` file to shift the source to the center before producing the final image. We used the elliptical Gaussian-fitting task `JMFIT` to obtain the component flux densities.

2.2. Emission-line Fitting

To fit the emission lines in the SDSS spectrum of KISSR 1494 and simultaneously obtain the stellar velocity dispersion from the absorption lines, we first separated the emission line spectrum from the underlying stellar continuum by the following steps. We corrected for reddening using SDSS tabulated $E(B-V)$ values (Schlegel et al. 1998) and then used the pPXF (penalized Pixel-Fitting stellar kinematics extraction) code by Cappellari & Emsellem (2004) to obtain the best fit model for the underlying stellar population. We corrected the spectrum for the redshift of the galaxy as listed in SDSS dr10. The `MILES` single stellar population models were used as templates of underlying stellar population as they cover a large range of metallicity ($M/H \sim -2.32$ to $+0.22$) and age (63 Myr to 17 Gyr). The stellar population contribution to the best fit template is $\sim 82\%$ and the remaining 18% accounts for the contribution from other components like, the power law component of AGN and Fe II lines. The stellar velocity dispersion obtained for KISSR 1494 from the absorption lines in the underlying stellar continuum is 206.6 ± 8.2 km s^{-1}.

The extracted pure emission line spectrum shows signatures of double peaks in prominent emission lines such as [S II], Hα, Hβ, Hγ, [O I], [O II], and [O III]. Our analysis used IDL programs that included the `MPFIT` function for fitting Gaussians to emission lines. We first modeled each [S II] doublet line as two Gaussians having equal line widths in velocity space. The [S II] model was used as a template to fit the narrow [N II] doublet lines as well as Hα and Hβ narrow lines. This procedure has been described by Reines et al. (2013). The separation between the centroids of the [N II] narrow components was held fixed and the flux of [N II] $\lambda6583$ to [N II] $\lambda6548$ was fixed at the theoretical value of 2.96. With the inclusion of a broad Hα component in addition to the two narrow components, the reduced χ^2 improved from 1.49 to 1.09. For the [O III] doublet lines an additional third broad component improved the fit by $\approx 20\%$ (χ^2 improved from 1.67 to 1.35). For the [O II] doublet lines, however, the broad component could be a consequence of the two blended/unresolved components in one of the doublet lines. The central wavelength of the broad component of Hα is redshifted by 7.23 ± 0.65 Å while [O III] is blueshifted by 2.64 ± 1.75 Å. The velocity widths of the broad Hα and [O III] components are 739.4 ± 26.3 km s^{-1} and 338.6 ± 53.0 km s^{-1}, respectively. The larger width of the Hα broad component compared to the [O III] broad component could signify a combination of Doppler broadening effects due to the BH and an outflow, both in Hα and the nearby [N II] doublet lines. The difference in the shifts of the central wavelengths of the broad components of [O III] and Hα could also be attributable to the same effect. All the prominent lines along with their best fitting components are shown in Figures 2 and 3; their details are noted in Table 1.
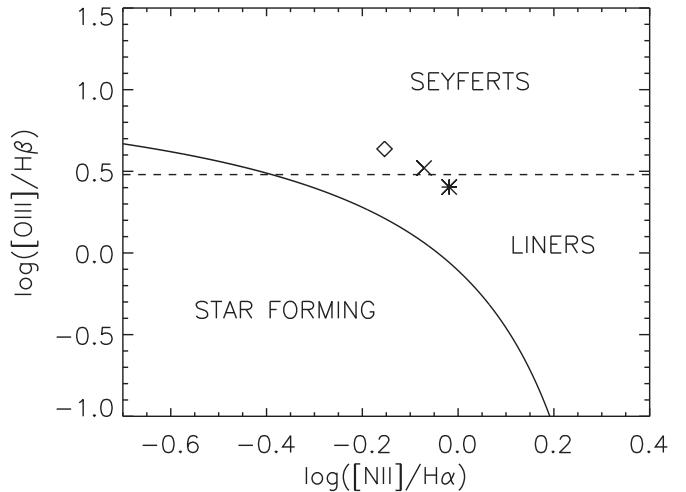

Figure 4. AGN diagnostic diagram for KISSR 1494. The $\diamond$ and $*$ symbols represent the line ratios for the separate components of the double peaked emission lines, while the $\times$ symbol represents line ratios derived from the total fluxes. All three line ratios are consistent with a Seyfert nucleus given the $\lesssim 10\%$ errors in line-fitting. It is evident however that KISSR 1494 lies close to the Seyfert–LINER boundary.

3. RESULTS

The AGN diagnostic diagram for KISSR 1494 confirms its Seyfert classification (Figure 4). The solid line is the demarcation between star formation (H II regions) and active nuclei from Kewley et al. (2001). The dashed horizontal line is the separation between Seyfert and LINER nuclei (e.g., Veilleux & Osterbrock 1987). We derived the line ratios log([O III], $\lambda5007$)/Hβ and log([N II] $\lambda6583$)/Hα in two ways: first, by taking the peaks separately and second, by combining all the emission as a mean value. Hence, Figure 4 has three points, with the mean line ratio being the central point in the plot (symbol $\times$). Keeping in mind that the errors in the line-fitting analysis can be $\lesssim 10\%$, all three line ratios are consistent with a Seyfert nucleus. However, it is also evident from Figure 4 that KISSR 1494 lies close to the Seyfert–LINER dividing line.

3.1. Parsec-scale Radio Emission

A single radio component was detected at 1.6 GHz (Figure 5), but not at 5 GHz. The radio component detected at 1.6 GHz has a peak intensity of $\sim 360\,\mu$Jy beam^{-1}, and an integrated flux density of $\sim 650\,\mu$Jy in a purely naturally weighted image (made with a `ROBUST` parameter of $+5$ in AIPS task `IMAGR`). The rms noise reached at 1.6 GHz was $\sim 6.5 \times 10^{-5}$ Jy beam^{-1}, making this a 10σ detection. At 5 GHz, where there was no source detection, a final rms noise of $\sim 3.5 \times 10^{-5}$ Jy beam^{-1} was reached. The deconvolved size of the radio component at 1.6 GHz was obtained from the purely naturally weighted image using the AIPS task `JMFIT`. This size is $\sim 7.5 \times 5$ mas, or $\sim 8 \times 6$ pc at the distance of the source.

In order to robustly examine the structure of the detected radio component at 1.6 GHz, we created images with different weighting schemes. Figure 5 shows the 1.6 GHz contour image made with uniform weighting using a `ROBUST` parameter of 0 in `IMAGR`. The rms noise in this image was $\sim 7.0 \times 10^{-5}$ Jy beam^{-1}. Figure 6 shows a superimposition of the two radio images made with pure natural weighting (with `ROBUST` = $+5$, in grayscale), and pure uniform weighting (with `ROBUST` = -5, in magenta-colored contours). The rms noise in the latter image was $\sim 1.3 \times 10^{-4}$ Jy beam^{-1}. All images have been

Table 1
Fitted Line Parameters

Line (1)	λ_0 (2)	$\lambda_c \pm$ Error (3)	$\Delta\lambda \pm$ Error (4)	$f_p \pm$ Error (5)	$\log f$ (6)	$\log L$ (7)
[S II]	6718.3	6716.36 ± 0.33	2.91 ± 0.08	51.85 ± 3.46	-14.42	40.45
		6722.16 ± 0.25	2.26 ± 0.18	43.43 ± 2.91	-14.61	40.26
[S II]	6732.7	6730.36 ± 0.33	2.92 ± 0.08	38.75 ± 2.67	-14.55	40.33
		6736.17 ± 0.25	2.27 ± 0.18	35.36 ± 2.32	-14.70	40.18
[N II]	6549.9	6548.25 ± 0.22	2.84 ± 0.08	75.26 ± 3.96	-14.27	40.60
		6553.84 ± 0.22	2.21 ± 0.18	52.69 ± 2.29	-14.54	40.34
[N II]	6585.3	6583.26 ± 0.22	2.86 ± 0.08	222.01 ± 3.96	-13.80	41.08
		6588.87 ± 0.22	2.22 ± 0.18	155.44 ± 2.29	-14.06	40.81
Hα	6564.6	6561.99 ± 0.26	2.85 ± 0.08	232.45 ± 13.17	-13.78	41.09
		6568.14 ± 0.23	2.21 ± 0.18	222.08 ± 5.81	-13.91	40.96
		6570.23 ± 0.65	16.19 ± 0.58	30.52 ± 3.04	-13.91	40.97
Hβ	4862.7	4860.37 ± 0.22	2.11 ± 0.08	52.59 ± 3.00	-14.55	40.32
		4865.11 ± 0.17	1.64 ± 0.18	51.55 ± 2.66	-14.67	40.20
[O III]	4960.3	4963.02 ± 2.66	2.47 ± 1.64	38.20 ± 58.23	-14.63	40.25
		4959.20 ± 4.72	2.92 ± 0.58	42.12 ± 72.03	-14.51	40.36
		4958.36 ± 1.75	5.60 ± 0.88	10.15 ± 7.79	-14.85	40.03
[O III]	5008.2	5011.00 ± 2.66	2.49 ± 1.64	112.70 ± 58.23	-14.15	40.72
		5007.13 ± 4.72	2.95 ± 0.58	124.26 ± 72.03	-14.04	40.84
		5006.04 ± 1.76	5.65 ± 0.88	29.96 ± 7.79	-14.37	40.50
[O I]	6302.0	6300.45 ± 2.81	2.41 ± 0.40	13.18 ± 14.36	-15.10	39.78
		6305.32 ± 3.13	2.56 ± 2.31	11.44 ± 4.44	-15.13	39.74
[O I]	6365.5	6364.45 ± 2.81	2.84 ± 0.94	4.39 ± 14.36	-15.51	39.37
		6369.37 ± 3.13	2.25 ± 2.74	3.81 ± 4.44	-15.67	39.21
[O II]	3727.1	3729.02 ± 1.01	1.62 ± 0.08	48.40 ± 53.66	-14.71	40.17
		3732.01 ± 0.44	1.26 ± 0.18	44.76 ± 23.89	-14.85	40.02
		3727.81 ± 1.67	2.67 ± 0.32	72.88 ± 37.55	-14.31	40.56
Hγ	4341.7	4338.60 ± 0.38	1.88 ± 0.08	16.03 ± 1.81	-15.12	39.75
		4343.22 ± 0.24	1.46 ± 0.18	19.10 ± 2.12	-15.16	39.72

Notes. Column 1: emission lines that were fitted with Gaussian components. Column 2: rest wavelength in vacuum in Å. Columns 3, 4: central wavelength and line width in Å along with respective errors. Column 5: peak line flux in units of $10^{-17}\,\mathrm{erg\,cm^{-2}\,s^{-1}\,\text{Å}^{-1}}$ with error. Column 6: logarithm of the total line flux in $\mathrm{erg\,cm^{-2}\,s^{-1}}$. Column 7: logarithm of the line luminosity in $\mathrm{erg\,s^{-1}}$.
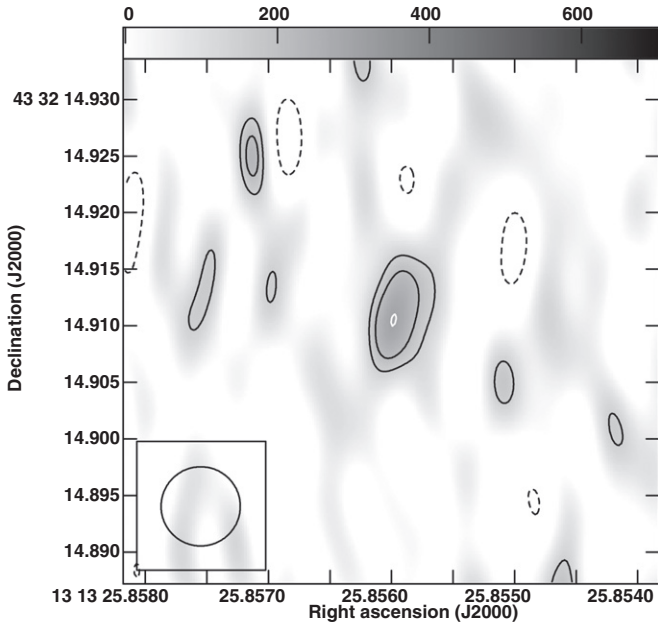

Figure 5. 1.6 GHz contour image of KISSR 1494. The contours are in percentage of the peak intensity and increase in steps of $\sqrt{2}$: the lowest contour and peak intensity are $\pm45\%$ and 3.2×10^{-4} Jy beam^{-1}, respectively. The inset at the bottom left corner shows the convolved beam of size 7×7 mas.
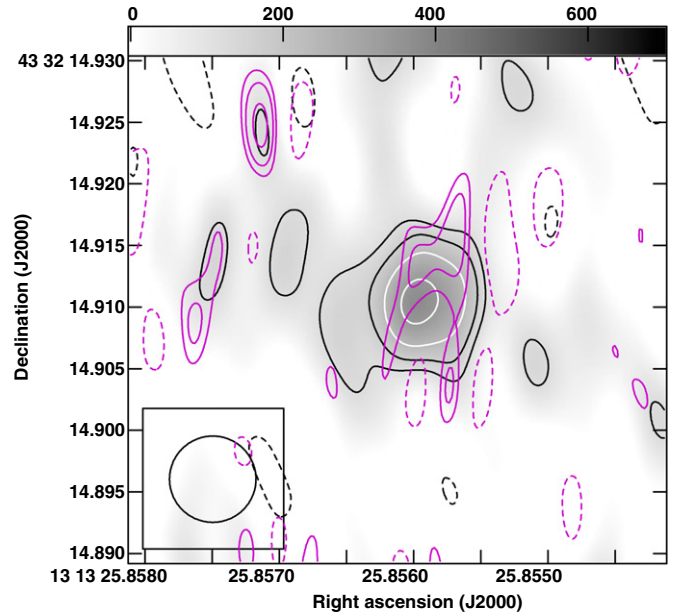

Figure 6. Superposition of the 1.6 GHz contour images made using pure natural weighting (in grayscale) and pure uniform weighting (in magenta). The contours are in percentage of the peak intensity and increase in steps of $\sqrt{2}$: the lowest contour levels are $\pm32\%$ for both the images, and the peak intensities are 3.7×10^{-4} Jy beam^{-1} for the grayscale and 6.7×10^{-4} Jy beam^{-1} for the magenta image. The convolved beam is of size 7×7 mas.

convolved with a circular beam of size 7 mas, which was the best intermediate value. The radio component is almost completely resolved out in the purely uniformly weighted image. The brightest emission that remains at the source position is at the $\sim 3\sigma$ level. While its integrity needs to be examined with more sensitive VLBI observations in the future, we have shown this image to highlight its lack of centrally concentrated emission.

Assuming that three times the rms noise at 5 GHz (= 3.5×10^{-5} Jy beam^{-1}) was an upper limit to the (undetected) source flux density, we derive the 1.6–5.0 GHz spectral index to be $\alpha = -1.5 \pm 0.5$, for a total source flux density of 650 μJy at 1.6 GHz. The rms noise at 1.6 and 5 GHz was used to estimate the spectral index error. This spectral index value is an underestimate because the 1.6 GHz data probes shorter (u, v) spacings than the 5 GHz data and could pick up flux that is missed at 5 GHz. Steep spectrum radio cores are not uncommon in Seyfert galaxies (e.g., Orienti & Prieto 2010; Kharb et al. 2010; Bontempi et al. 2012). The steep radio spectrum rules out thermal or free–free emission as the radiation mechanism and instead supports a non-thermal origin.

The brightness temperature (in Kelvin) of the radio component at 1.6 GHz was estimated using the relation,

$$T_B = 1.8 \times 10^9 (1+z) \left(\frac{S_\nu}{1\,\text{mJy}}\right) \left(\frac{\nu}{1\,\text{GHz}}\right)^{-2} \left(\frac{\theta_1 \theta_2}{\text{mas}^2}\right)^{-1},$$

where θ_1, θ_2 are the major, minor axes of the best-fitting elliptical Gaussian for a resolved radio component (Ulvestad et al. 2005). T_B of the radio component is $\sim 1.4 \times 10^7$ K. This suggests that the radio emission is related to an AGN rather than a nuclear starburst. Starbursts typically exhibit brightness temperatures of $< 10^5$ K (Condon et al. 1991).

Assuming equipartition of energy between relativistic particles and the magnetic field (Burbidge 1959), we obtained the minimum pressure, and the particle energy (electrons and protons) at minimum pressure using the relations in O'Dea & Owen (1987),

$$L_{\text{rad}} = 1.2 \times 10^{27} D_L^2 S \nu^{-\alpha} (1+z)^{-(1+\alpha)} \left(\nu_u^{1+\alpha} - \nu_l^{1+\alpha}\right)(1+\alpha)^{-1},$$
$$P_{\text{min}} = (2\pi)^{-3/7}(7/12)[c_{12} L_{\text{rad}}(1+k)(\phi V)^{-1}]^{4/7},$$
$$B_{\text{min}} = [2\pi(1+k)c_{12} L_{\text{rad}}(\phi V)^{-1}]^{2/7},$$
$$E_{\text{min}} = [\phi V (2\pi)^{-1}]^{3/7} [L_{\text{rad}}(1+k)c_{12}]^{4/7},$$

where L_{rad} is the radio luminosity in erg s^{-1}, D_L is the luminosity distance in Mpc, z is the source redshift, S is the total flux density in Jy, ν is frequency in Hz, ν_u and ν_l are the upper and lower frequency cutoffs in Hz, respectively, P_{min} is the minimum pressure in dynes cm^{-2}, k is the ratio of the relativistic proton to relativistic electron energy, V is the source volume, c_{12} is a constant depending on the spectral index and frequency cutoffs, ϕ is the volume filling factor, B_{min} is the magnetic field at minimum pressure in G, and E_{min} is the particle energy (electrons and protons) at minimum pressure in ergs. The total radio luminosity was estimated assuming that the radio spectrum extends from (ν_l) 10 MHz to (ν_u) 100 GHz with a spectral index of $\alpha = -1$. Furthermore, it was assumed that $k = 1$. Table 2 lists equipartition estimates for plasma filling factors of unity and 0.5 (e.g., Blustin & Fabian 2009). The total energy in particles and fields, E_{tot}, is estimated as $E_{\text{tot}} = 1.25 \times E_{\text{min}}$, while the total energy density, U_{tot}, in erg cm^{-3} is $= E_{\text{tot}}(\phi V)^{-1}$.

The lifetime of electrons in the radio component undergoing both synchrotron radiative and inverse-Compton losses on

Table 2
Equipartition Estimates

L_{rad}	ϕ	P_{min}	E_{min}	B_{min}	E_{tot}	U_{tot}	t_e
1.4×10^{41}	0.5	5.2×10^{-6}	3.2×10^{52}	7.4	4.0×10^{52}	1.1×10^{-5}	980
1.4×10^{41}	1.0	3.5×10^{-6}	4.3×10^{52}	6.1	5.4×10^{52}	7.4×10^{-6}	1320

Notes. Column 1: total radio luminosity in erg s^{-1}. Column 2: plasma filling factor. Column 3: minimum pressure in dynes cm^{-2}. Column 4: minimum energy in ergs. Column 5: minimum B-field in mG. Column 6: total energy in particles and fields, E_{tot} ($= 1.25 \times E_{\text{min}}$) in ergs. Column 7: total energy density, $U_{\text{tot}} = E_{\text{tot}}(\phi V)^{-1}$ in erg cm^{-3}. Column 8: electron lifetimes in yr. See Section 3.1 for details.

cosmic microwave background (CMB) photons was estimated using the relation (van der Laan & Perola 1969),

$$t_e \simeq 2.6 \times 10^4 \frac{B^{1/2}}{B^2 + B_r^2} \frac{1}{[(1+z)\nu_b]^{1/2}} \text{ yr},$$

where B was assumed to be the equipartition magnetic field B_{min}, and the break frequency ν_b was assumed to be 1.6 GHz. The magnetic field equivalent to the radiation, which was assumed to be predominantly CMB photons, B_r, was estimated using the relation, $B_r \simeq 4 \times 10^{-6}(1+z)^2$ G. The B_{min} values of a few mG, log U_{tot} of ~ -5.0 and electron lifetimes of $\sim$1000 yr are similar to estimates derived for the parsec-scale radio jets in Seyfert galaxies (e.g., Kharb et al. 2010, 2014a; Orienti & Prieto 2010; Bontempi et al. 2012). The significance of this finding will be discussed in Section 4.4.

3.2. Star Formation Rate

While the high brightness temperature supports an AGN origin for the radio emission in KISSR 1494, here we test the idea that the radio emission is star formation related. If we assume that all of the radio luminosity is attributable to star formation, a star formation rate (SFR) can be derived using the relation (Condon 1992),

$$\text{SFR}\,(M_\odot\,\text{yr}^{-1}) = \text{L(W\,Hz}^{-1})/5.3 \times 10^{21}\,\nu(\text{GHz})^\alpha.$$

We find that the upper limit to the SFR (for stellar masses $\geqslant 5\,M_\odot$; see Condon 1992) from the 1.4 GHz luminosity (= 1.72×10^{23} W Hz^{-1}) obtained in the kiloparsec-scale FIRST image is $\approx 43\,M_\odot$ yr^{-1} for a spectral index of $\alpha = -0.8$.

The SFR can also be estimated from the narrow Hα line. Adding the flux of the two narrow components of Hα (= 2.9×10^{-14} erg cm^{-2} s^{-1}) and following the relation in Kennicutt (1998),

$$\text{SFR}\,(M_\odot\,\text{yr}^{-1}) = 7.9 \times 10^{-42}\,L_{[\text{H}\alpha]}\,(\text{erg s}^{-1}),$$

we derive a SFR of $\sim 1.7\,M_\odot$ yr^{-1} for $L_{\text{H}\alpha} = 2.16 \times 10^{41}$ erg s^{-1}. The SFR in KISSR 1494 derived from its optical spectrum therefore appears to be fairly low, and cannot account for the observed radio emission on kiloparsec-scales, which require the SFR to be $> 40\,M_\odot$ yr^{-1}. This finding supports the idea that the radio emission on kiloparsec-scales in KISSR 1494 is AGN-outflow related.

3.3. SMBH Mass and Eddington Rate

Since equal peaked emission lines could arise in a rotating disk around the SMBH (Smith et al. 2012), we use the suggestion of a disk to derive the dynamical mass of the SMBH in

Table 3
Black Hole Mass Estimates

Method	M_{BH}	Caveat
Dynamical	$3.8 \times 10^7 \, M_\odot$	Arbitrary disk-size from radio data
M_{BH}–$\sigma_\star$	$1.4 \times 10^8 \, M_\odot$	Large scatter in relation for late-type galaxies
Broad Hα	$3.7 \times 10^6 \, M_\odot$	Broad component could signify outflow

KISSR 1494. Using the disk radius r and the mean rotation speed $\langle v \rangle$, the mass of the SMBH can be derived as $M_{BH} = (v^2 r/G)$. We use the difference between the double peaks in the Hα and Hβ lines ($\Delta\lambda_1$ and $\Delta\lambda_2$) to determine v, where $2v = (1/2)[c\Delta\lambda_1/6562.8) + (c\Delta\lambda_2/4861.36)]$, and the denominators are the respective rest wavelengths in air. For $\Delta\lambda_1 = 6.15$ Å and $\Delta\lambda_2 = 4.74$ Å, we obtain $v = 142.93$ km s^{-1}. As the compact radio source has a dimension of 7.5×5 mas, we adopt an *arbitrary* disk diameter of 7.5 mas (~ 8 pc). This yields a BH mass of $M_{BH} = 3.8 \times 10^7 \, M_\odot$ for KISSR 1494.

The SMBH mass can also be estimated from the width and the luminosity of the broad component of the Hα line (Figure 2, Table 1). This method assumes that the broad component originates in the BLR and is not due to outflows (Reines et al. 2013), and that the BLR clouds are in virial equilibrium with the SMBH (Kaspi et al. 2005). Using the relation for BH mass from Reines et al. (2013) for a scale factor (ϵ) of unity:

$$\log\left(\frac{M_{BH}}{M_\odot}\right) = 6.57 + 0.47 \log(L_{H\alpha}) + 2.06 \log(\text{FWHM}_{H\alpha}),$$

where Hα line luminosity is in units of 10^{42} erg s^{-1} and FWHM in units of 10^3 km s^{-1}, we obtain $M_{BH} = 3.7 \times 10^6 \, M_\odot$, for $L_{H\alpha} = 9.26 \times 10^{40}$ erg s^{-1}. However, a broad component is also observed in both the [O III] $\lambda\lambda 4959, 5007$ lines, which could be attributable to outflows related either to the AGN or nuclear star-formation (e.g., Esquej et al. 2014). If the broad Hα line likewise had a significant outflow component, this BH mass estimate would be unreliable.

The bulge stellar velocity dispersion as derived by our line-fitting is $\sigma_\star = 206.6 \pm 8.2$ km s^{-1}. Following the M_{BH}–$\sigma_\star$ relation for late-type galaxies (McConnell & Ma 2013):

$$\log\left(\frac{M_{BH}}{M_\odot}\right) = 8.07 + 5.06 \log\left(\frac{\sigma_\star}{200 \text{ km s}^{-1}}\right),$$

we derive a BH mass, $M_{BH} = 1.4 \pm 1.0 \times 10^8 \, M_\odot$, which is ≈ 4 times larger than the dynamical mass limit derived above. It is evident that the M_{BH}–$\sigma_\star$ relation has a lot of scatter when it comes to late-type galaxies.

All three estimates of BH mass are very crude. For the lack of a more reliable measurement, we have adopted the BH mass derived from the M_{BH}–$\sigma_\star$ relation in the rest of the paper. In Table 3 we list all the BH mass estimates along with their caveats.

We use the combined flux of the narrow components of the [O III] $\lambda 5008$ line (= 1.21×10^{41} erg s^{-1}) to estimate the bolometric luminosity (L_{bol}) using the relation from Heckman et al. (2004): $L_{bol}/L_{[O\,III]} \approx 3500$, where $L_{[O\,III]}$ is the monochromatic continuum luminosity at a 5000 Å rest frame. We derive $L_{bol} = 4.2 \times 10^{44}$ erg s^{-1}. For a BH mass of $1.4 \times 10^8 \, M_\odot$, the Eddington luminosity ($\equiv 1.25 \times 10^{38} M_{BH}/M_\odot$) is $\approx 1.7 \times 10^{46}$ erg s^{-1} and the Eddington rate ($\equiv L_{bol}/L_{Edd}$) is ~ 0.02. The accretion rate in KISSR 1494 seems to be typical of Seyfert galaxies in the literature (e.g., Ho 2008). In short, the double peaked emission line Seyfert KISSR 1494 does not distinguish itself from other Seyfert galaxies in terms of its BH mass and accretion properties.

4. DISCUSSION

A single steep spectrum radio component is detected in the double peaked emission line Seyfert galaxy, KISSR 1494. The spectrum does not favor thermal free–free emission, but rather optically thin synchrotron emission. While steep spectrum radio cores are fairly prevalent in Seyfert galaxies, they may represent a different phenomena compared to the typical flat/inverted spectra radio cores observed in radio-loud sources and even many Seyfert galaxies, that are traditionally regarded as the synchrotron-self-absorbed unresolved bases of radio jets. The high brightness temperature of $T_B \sim 1.4 \times 10^7$ K also favors a non-thermal AGN-related origin rather than a nuclear starburst which is expected to have $T_B < 10^5$ K. Additionally, the low SFR derived from the optical spectrum (SFR $\sim 1.7 \, M_\odot$ yr^{-1}), does not support the idea of the kiloparsec-scale radio emission in KISSR 1494 being starburst related, which requires an SFR $> 40 \, M_\odot$ yr^{-1}. We discuss below the favored mechanisms for explaining double peaked emission lines in AGNs in the context of high resolution radio observations of KISSR 1494.

4.1. The Binary SMBH Scenario

The presence of a single radio component per se does not rule out the binary BH scenario. One possibility could be that the two BHs have separations less than the size of the detected radio component, i.e., if they are separated by <8 pc. However in this case, the NLR clouds giving rise to the double peaks will have to be restricted to those spatial scales as well, making this an unattractive proposition. The NLR clouds typically exist on spatial scales of tens to hundreds of parsecs from the central engine (e.g., Crenshaw et al. 2000). In addition, it is unclear what media (equivalent to dusty tori around BLR clouds) could shield the spatially extended NLR clouds of the two BHs from mixing and losing their individual identities.

An alternate scenario could be that a second BH is indeed present, but has associated radio emission that is below the rms noise in the final image ($\sim 6.5 \times 10^{-5}$ Jy beam^{-1} at 1.6 GHz). There is a well established correlation between the core radio luminosity at 5 GHz (L_5, W Hz^{-1}) and the BH mass for nearby early-type galaxies (Franceschini et al. 1998): $L_5 \propto M_{BH}^{2.73}$. What is more relevant to KISSR 1494 is that for a handful of late-type galaxies considered in this study, the BH mass exponent is still close to 2.7. Assuming the 1.6–5.0 GHz core spectral index to be -1, we estimate that the upper limit to the radio luminosity at 5 GHz from the second BH would be $\sim 1.5 \times 10^{20}$ W Hz^{-1}. From the L_5–M_{BH} relation, this implies that the mass of the second BH would be $\lesssim 2.5 \times 10^7 \, M_\odot$. At the upper limit, this BH mass lies close to the M_{BH}–$\sigma_\star$ mass of the primary BH (that emits at radio frequencies) within error limits. It would be surprising though if a major merger took place in KISSR 1494 in its past and left no tell-tale signatures of a disturbance, like tidal tails, shells or loops. In addition, this merger apparently left the spiral features of the host galaxy intact. Major mergers of spiral galaxies are expected to lead to the formation of elliptical galaxies (e.g., Schweizer 1982). This disfavors the suggestion of a second BH with a mass nearly equal to the primary BH (with the associated radio emission), but having only faint (undetectable) radio emission. It is also instructive to remember that Burke-Spolaor (2011) found only two binary AGNs in a sample of 3114 radio-bright AGNs observed with VLBI, attesting to the rarity of sources with binary back holes.

An important caveat to the discussion above must be mentioned. It is possible that the detected radio component at

1.6 GHz is not coincident with the position of the central SMBH, but is instead a bright portion of a radio outflow, like a compact jet knot or a "hot spot." However, it is not possible to verify this with the present day optical telescopes. Only a more sensitive VLBI study at multiple wavelengths may detect either more radio components from the radio outflow or reveal the spectral index information with greater confidence, and thereby elucidate the true nature of the detected radio feature. For the purposes of this paper, we have assumed that the detected radio component is indeed coincident with the SMBH in KISSR 1494.

4.2. The Rotating Disk Scenario

Smith et al. (2012) have proposed that equal-peaked AGNs, of which KISSR 1494 is an example, could have their line emission originating in a rotating ring with relatively little gas at small radii. The fact that the radio component detected at 1.6 GHz in KISSR 1494 is not compact and gets completely resolved out in some image weighting schemes (see Figure 6) can be reconciled with the fact that the radio emission is from a disk or a ring/torus. Could the same rotating disk or ring/torus give rise to the double peaked emission lines? This is unlikely because of the small size of the radio feature ($\sim 8 \times 6$ pc)—the NLR clouds are expected to be distributed on much larger 10–100 pc scales, extending beyond the parsec-scale torus. However, it is possible that the disk is much more extended than the region probed by VLBI and the NLR clouds form part of the outer regions of this disk. The missing diffuse radio emission going from kiloparsec to parsec-scales could also arise in an extended disk emitting at radio frequencies. Mulchaey et al. (1996) have demonstrated that if the NLR is in a disk then the V-shaped ionization cones will always be observed in Seyfert galaxies, irrespective of our line of sight being inside or outside of the cones. The prevalence of ionization cones therefore favors NLR disks.

Gallimore et al. (2004) have suggested that the flat/inverted spectrum radio core in the Seyfert galaxy NGC 1068 is thermal bremsstrahlung (free–free) emission from the inner hot ionized edge of the torus. Roy et al. (1998) have discussed the possibility that the radio core in NGC 1068 is direct synchrotron emission from the torus instead. The steep spectrum along with the moderate brightness temperature $T_B \sim 10^7$ K in the radio core of KISSR 1494 does not favor synchrotron self-absorption from the torus as an explanation, but rather optically thin synchrotron emission. For synchrotron self-absorption to occur, $T_B > 10^9$ K is typically required. Steep-spectrum parsec-scale radio emission from another Seyfert galaxy, NGC 4388, has been suggested to originate in a disk (Giroletti & Panessa 2009). The size of the radio emitting disk in NGC 1068 is ~ 0.4 pc with a $T_B = 2.6 \times 10^6$ K, while the size of the radio disk in NGC 4388 is ~ 0.5 pc with a $T_B = 1.3 \times 10^6$ K. The NLR in NGC 1068 and NGC 4388 are probably not disky because their SDSS spectra do not exhibit double-peaked emission lines, unless their NLR disks are nearly face-on. If the radio component in KISSR 1494 is indeed emission from a disk, its size is at least 10 times larger than disks in NGC 1068 and NGC 4388. Its brightness temperature is five to ten times higher as well. The significance of this difference is unclear at present.

4.3. The Radio Outflow Scenario

If a radio outflow impacts the gas clouds in the NLR, then the approaching and receding emission-line gas clouds could give rise to the double peaked emission line spectra. The lack of a clear parsec-scale core-jet structure is not consistent with

a powerful radio outflow in KISSR 1494. However, a broad wind-like parsec-scale radio outflow cannot be ruled out.

As noted in Section 1, the total radio flux density of KISSR 1494 with the VLA FIRST survey at 1.4 GHz is ~ 23 mJy. This flux density drops to 0.65 mJy at 1.6 GHz with VLBI (present study). Hence most of the radio flux density comes from a diffuse radio component on scales between a few arcseconds and 10 mas. AGN-driven outflows have indeed been observed on scales of a few kiloparsec in Seyfert galaxies, especially with sensitive radio observations (e.g., Kharb et al. 2006, 2014b; Gallimore et al. 2006). If we assume that the kiloparsec-scale emission is lobe emission from a broad AGN outflow in KISSR 1494, then we can estimate the time-averaged kinetic power (Q) of this outflow following the relations in Punsly & Zhang (2011) for radio-powerful sources (see also Willott et al. 1999):

$$Q \approx 1.1 \times 10^{45}[(1+z)^{1+\alpha} Z^2 F_{151}]^{6/7} \text{erg s}^{-1},$$
$$Z \equiv 3.31 - 3.65[(1+z)^4 - 0.203(1+z)^3$$
$$+ 0.749(1+z)^2 + 0.444(1+z) + 0.205]^{-0.125},$$

where F_{151} is the 151 MHz flux density and z is the source redshift. We derive F_{151} using the 1.4 GHz flux density from FIRST and a lobe spectral index of $\alpha = -0.8$, and obtain a kinetic power of $Q \approx 1.5 \times 10^{42}$ erg s^{-1}. This Q value is typical of outflows in low-luminosity AGNs (e.g., Mezcua & Prieto 2014).

Blundell & Kuncic (2007) have suggested that the radio core emission in radio-quiet quasars is thermal free–free emission from a slow dense disk wind. The radio data of KISSR 1494 are consistent with a disk wind that emits synchrotron emission instead. It could indeed be wind emission from the tenuous corona region above the accretion disk, which has a sufficient supply of relativistic electrons and strong magnetic fields (e.g., Merloni & Fabian 2002; Laor & Behar 2008). In this scenario, the radio emission does come from a less collimated outflow compared to a relativistic jet. As mentioned by Marscher (2006), the corona itself could be the low altitude portion of a wind flowing from the accretion disk. The double-peaked emission lines in the source could also be explained if the NLR clouds are a part of this broader outflow. Even the equal peaks of the Hα and Hβ emission lines can be explained if they arise in a highly symmetric outflow close to the central engine, whose intensities are not significantly affected by dust obscuration.

4.4. Disk versus Outflow

We conclude that the radio continuum emission and the double-peaked emission lines in the spectrum of KISSR 1494 are consistent primarily with two explanations: (A) the mas-scale radio emission is the parsec-scale base of a synchrotron wind from the magnetized corona above the accretion disk. The NLR clouds are also a part of this outflow and extend to larger scales, probably of the order of tens to hundreds of parsecs (e.g., Crenshaw et al. 2000; Ruiz et al. 2005), and (B) the milliarcsec-scale radio emission comes from the (static, as in not outflowing) inner ionized edge of the accretion disk or torus; this disk extends to tens or hundreds of parsecs and also incorporates the rotating NLR clouds. In both these cases the radio emission is from the synchrotron mechanism. While the extensive literature on the presence of parsec-scale radio outflows in Seyferts (e.g., Giroletti & Panessa 2009) supports explanation A, the fact that KISSR 1494 is an "equal-peaked" AGN supports the disk explanation B. However, as

mentioned in Section 4.3, a highly symmetric AGN-driven NLR outflow where the line intensities from the receding flow are not significantly obscured by dust, could also support explanation A in "equal-peaked" AGNs. Therefore, although our present data cannot clearly distinguish between explanations A and B, there appears to be more supporting evidence for explanation A, i.e., a non-thermal coronal disk wind. Finally, the radio and NLR emission may be decoupled. The radio emission may come from an outflow while the NLR may be in a disk, and vice versa.

If the radio core in KISSR 1494 is indeed an outflowing coronal wind, it is interesting to note that its properties (magnetic field strength, total energy density, electron lifetime, kinetic power) are no different from the radio "jet" properties derived in other Seyfert galaxies. This supports the idea that radio "jets" and outflowing coronal winds are indistinguishable in Seyferts. The implication of this finding needs to be explored further.

5. SUMMARY AND CONCLUSIONS

We have carried out phase-referenced VLBI observations at 1.6 and 5 GHz of the double emission line peaked Seyfert galaxy, KISSR 1494. The primary findings are as follows.

1. A single radio component of size 7.5×5.1 mas ($\sim 8 \times 6$ pc) is observed at 1.6 GHz. There is no detection at 5 GHz. This implies a radio spectral index steeper than -1.5 ± 0.5. The high brightness temperature of the radio component ($T_B \sim 1.4 \times 10^7$ K) and the steep radio spectrum suggest that it is non-thermal synchrotron emission, rather than thermal free–free emission.

2. The SFR derived from the Hα line in the optical spectrum ($\sim 1.7\,M_\odot$ yr^{-1}) is too low to account for the radio luminosity on kiloparsec-scales which requires a SFR greater than $\sim 40\,M_\odot$ yr^{-1}. This supports the idea that the radio emission is AGN-outflow related.

3. The presence of a single radio core could per se be construed as being inconsistent with the binary BH picture for producing double peaked emission lines in this galaxy. However, the suggestions that binary BHs exist within the ~ 8 pc region of the detected radio component, or that one of the BHs is "radio-quiet," could still hold. These suggestions are not without their own characteristic difficulties.

4. The twin peaks observed in Hα, Hβ, and [S II] are identical, suggesting that the NLR clouds could be part of a rotating disk. That the radio component gets completely resolved out in certain image weighting schemes can be reconciled with the fact that the radio emission is from a disk or a torus.

5. The lack of a clear core-jet structure is inconsistent with a strong, collimated radio outflow being the primary mechanism for the production of the double emission line peaks. However, a broad outflow arising in an accretion disk corona is favored by our data.

6. From the M_{BH}–$\sigma_\star$ relation for late-type galaxies, a BH mass of $M_{BH} = 1.4 \pm 1.0 \times 10^8\,M_\odot$ is derived, accreting at an Eddington rate of ~ 0.02. In terms of its BH mass and accretion properties, as well as the magnetic field strength and "minimum" total energy (charged particles and magnetic fields) derived under the equipartition assumption, the double peaked emission line Seyfert KISSR 1494 does not distinguish itself from other Seyfert galaxies.

7. To summarize, the VLBI data are consistent with two explanations: the radio emission is the parsec-scale base of a synchrotron wind from the magnetized corona above the accretion disk, or the radio emission comes from the inner ionized edge of the accretion disk or torus that is not outflowing. In the first case, the NLR clouds could also be a part of this broad outflow, while in the latter, the NLR clouds could form a part of an extended disk beyond the torus. It is also possible that the radio emission comes from an outflow while the NLR clouds are in a disk, or vice versa. While with the present data, it is not possible to clearly distinguish between these scenarios, there appears to be greater circumstantial evidence supporting the coronal wind picture in KISSR 1494. From the kiloparsec-scale radio emission, the time-averaged kinetic power of this outflow is estimated to be $Q \approx 1.5 \times 10^{42}$ erg s^{-1}, a value typical of radio outflows in low-luminosity AGNs. This suggests that radio "jets" and outflowing coronal winds are indistinguishable in Seyferts.

REFERENCES

Aguerri, J. A. L., Balcells, M., & Peletier, R. F. 2001, A&A, 367, 428
Barnes, J. E., & Hernquist, L. 1992, ARA&A, 30, 705
Baum, S. A., O'Dea, C. P., Dallacassa, D., de Bruyn, A. G., & Pedlar, A. 1993, ApJ, 419, 553
Blundell, K. M., & Kuncic, Z. 2007, ApJL, 668, L103
Blustin, A. J., & Fabian, A. C. 2009, MNRAS, 396, 1732
Bontempi, P., Giroletti, M., Panessa, F., Orienti, M., & Doi, A. 2012, MNRAS, 426, 588
Burbidge, G. R. 1959, ApJ, 129, 849
Burke-Spolaor, S. 2011, MNRAS, 410, 2113
Cappellari, M., & Emsellem, E. 2004, PASP, 116, 138
Condon, J. J. 1992, ARA&A, 30, 575
Condon, J. J., Huang, Z., Yin, Q. F., & Thuan, T. X. 1991, ApJ, 378, 65
Crenshaw, D. M., Kraemer, S. B., Hutchings, J. B., et al. 2000, AJ, 120, 1731
Deane, R. P., Paragi, Z., Jarvis, M. J., et al. 2014, Natur, 511, 57
Esquej, P., Alonso-Herrero, A., González-Martín, O., et al. 2014, ApJ, 780, 86
Fabbiano, G., Wang, J., Elvis, M., & Risaliti, G. 2011, Natur, 477, 431
Fischer, T. C., Crenshaw, D. M., Kraemer, S. B., et al. 2011, ApJ, 727, 71
Franceschini, A., Vercellone, S., & Fabian, A. C. 1998, MNRAS, 297, 817
Fu, H., Myers, A. D., Djorgovski, S. G., & Yan, L. 2011, ApJ, 733, 103
Fu, H., Yan, L., Myers, A. D., et al. 2012, ApJ, 745, 67
Gabányi, K. É., Frey, S., Xiao, T., et al. 2014, MNRAS, 443, 1509
Gallimore, J. F., Axon, D. J., O'Dea, C. P., Baum, S. A., & Pedlar, A. 2006, AJ, 132, 546
Gallimore, J. F., Baum, S. A., & O'Dea, C. P. 2004, ApJ, 613, 794
Giroletti, M., & Panessa, F. 2009, ApJL, 706, L260
Gitti, M., Giroletti, M., Giovannini, G., Feretti, L., & Liuzzo, E. 2013, A&A, 557, L14
Heckman, T. M., Kauffmann, G., Brinchmann, J., et al. 2004, ApJ, 613, 109
Ho, L. C. 2008, ARA&A, 46, 475

Ho, L. C., & Peng, C. Y. 2001, ApJ, 555, 650
Hota, A., & Saikia, D. J. 2006, MNRAS, 371, 945
Kaspi, S., Maoz, D., Netzer, H., et al. 2005, ApJ, 629, 61
Kennicutt, R. C., Jr. 1998, ARA&A, 36, 189
Kewley, L. J., Heisler, C. A., Dopita, M. A., & Lumsden, S. 2001, ApJS, 132, 37
Kharb, P., Hota, A., Croston, J. H., et al. 2010, ApJ, 723, 580
Kharb, P., O'Dea, C. P., Baum, S. A., Colbert, E. J. M., & Xu, C. 2006, ApJ, 652, 177
Kharb, P., O'Dea, C. P., Baum, S. A., et al. 2014a, MNRAS, 440, 2976
Kharb, P., Singh, V., Gallimore, J. F., & Ishwara-Chandra, C. H. 2014b, arXiv:1402.1577
Komossa, S., Burwitz, V., Hasinger, G., et al. 2003, ApJL, 582, L15
Kormendy, J., & Ho, L. C. 2013, ARA&A, 51, 511
Laor, A., & Behar, E. 2008, MNRAS, 390, 847
Malzac, J., Beloborodov, A. M., & Poutanen, J. 2001, MNRAS, 326, 417
Markoff, S., Nowak, M. A., & Wilms, J. 2005, ApJ, 635, 1203
Marscher, A. P. 2006, AN, 327, 217
McConnell, N. J., & Ma, C.-P. 2013, ApJ, 764, 184
Merloni, A., & Fabian, A. C. 2002, MNRAS, 332, 165
Mezcua, M., & Prieto, M. A. 2014, ApJ, 787, 62
Mulchaey, J. S., Wilson, A. S., & Tsvetanov, Z. 1996, ApJ, 467, 197
Nagar, N. M., Falcke, H., & Wilson, A. S. 2005, A&A, 435, 521
O'Dea, C. P., & Owen, F. N. 1987, ApJ, 316, 95
Orienti, M., & Prieto, M. A. 2010, MNRAS, 401, 2599
Panessa, F., & Giroletti, M. 2013, MNRAS, 432, 1138
Punsly, B., & Zhang, S. 2011, ApJL, 735, L3
Reines, A. E., Greene, J. E., & Geha, M. 2013, ApJ, 775, 116

Rodriguez, C., Taylor, G. B., Zavala, R. T., et al. 2006, ApJ, 646, 49
Rosario, D. J., Shields, G. A., Taylor, G. B., Salviander, S., & Smith, K. L. 2010, ApJ, 716, 131
Roy, A. L., Colbert, E. J. M., Wilson, A. S., & Ulvestad, J. S. 1998, ApJ, 504, 147
Roy, A. L., Ulvestad, J. S., Wilson, A. S., et al. 2000, in Perspectives on Radio Astronomy: Science with Large Antenna Arrays, ed. M. P. van Haarlem (Dwingeloo, Netherlands: ASTRON), 173
Ruiz, J. R., Crenshaw, D. M., Kraemer, S. B., et al. 2005, AJ, 129, 73
Schlegel, D. J., Finkbeiner, D. P., & Davis, M. 1998, ApJ, 500, 525
Schweizer, F. 1982, ApJ, 252, 455
Shen, Y., Liu, X., Greene, J. E., & Strauss, M. A. 2011, ApJ, 735, 48
Singh, V., Ishwara-Chandra, C. H., Wadadekar, Y., Beelen, A., & Kharb, P. 2015, MNRAS, 446, 599
Smith, K. L., Shields, G. A., Salviander, S., Stevens, A. C., & Rosario, D. J. 2012, ApJ, 752, 63
Steinmetz, M., & Navarro, J. F. 2002, NewA, 7, 155
Stevenson, S. L., Salzer, J. J., Sarajedini, V. L., & Moran, E. C. 2002, AJ, 124, 3465
Ulvestad, J. S., Antonucci, R. R. J., & Barvainis, R. 2005, ApJ, 621, 123
van der Laan, H., & Perola, G. C. 1969, A&A, 3, 468
Veilleux, S., & Osterbrock, D. E. 1987, ApJS, 63, 295
Volonteri, M., Haardt, F., & Madau, P. 2003, ApJ, 582, 559
Wegner, G., Salzer, J. J., Jangren, A., Gronwall, C., & Melbourne, J. 2003, AJ, 125, 2373
Willott, C. J., Rawlings, S., Blundell, K. M., & Lacy, M. 1999, MNRAS, 309, 1017
Wrobel, J. M., Walker, R. C., & Fu, H. 2014, ApJL, 792, L8
Zang, T. A., & Hohl, F. 1978, ApJ, 226, 521